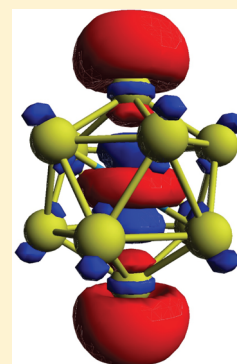


Jahn–Teller Instability of Icosahedral $[\text{W@Au}_{12}]^-$ Tohru Sato,^{*,†} Erwin Lijnen,[‡] and Arnout Ceulemans[‡][†]Department of Molecular Engineering, Graduate School of Engineering and Unit of Elements Strategy Initiative for Catalysts & Batteries, Kyoto University, Nishikyo-ku, Kyoto 615-8510, Japan[‡]Division of Quantum Chemistry and Physical Chemistry, Department of Chemistry, Katholieke Universiteit Leuven, Celestijnenlaan 200F, B-3001 Heverlee, Belgium

S Supporting Information

ABSTRACT: The anionic state of the icosahedral W@Au_{12} cluster offers a rare example of a Jahn–Teller (JT) instability in an icosahedral fourfold degenerate Γ_8 spinor level. The JT energy splittings of the ground Γ_8 and excited sixfold degenerate Γ_9 splittings in the vicinity of the degeneracy point are calculated with relativistic density functional theory. The results are very well explained by a first-order coupling model, based on the orbital instability of the spherical d -shell of the cluster. In addition the pentagonal JT minimum has been determined. It presents a remarkable example of an auro-sandwich type compound.



1. INTRODUCTION

The anionic $[\text{W@Au}_{12}]^-$ offers a rare example of an icosahedral Jahn–Teller instability in the presence of substantial spin–orbit coupling. The corresponding JT model Hamiltonians for fourfold and sixfold degenerate spinor representations have only quite recently been constructed.¹ The purpose of the present study is to confront the model treatment with relativistic density functional theory (DFT) computations. The calculations concern the vicinity of the degeneracy point and provide the first-order level splittings from which the vibronic coupling constants can be extracted. The perfect icosahedral cage has the unique property that its vibrations can be classified according to the parent S_6 symmetric group of the permutations of the six fivefold directions.² This symmetry provides a solution to the inherent product multiplicity problem of the JT Hamiltonians and will be used to compute the two coupling channels separately. In addition we also examine the minimal energy distorted structure at the bottom of the JT surface. This structure reveals an interesting alternative bonding scheme, with the gold atoms in the role of aromatic ligands in a sandwich complex.

2. MODEL OF THE JAHN–TELLER INSTABILITY IN W@Au_{12}^-

2.1. Bonding Scheme. Pyykkö and Runeberg predicted W@Au_{12} to be a stable closed-shell cluster with I_h symmetry.^{3,4} In I_h the frontier $6s$ orbitals of the 12 gold atoms span $a_g + t_{1u} + h_g + t_{2u}$ symmetries as shown in Figure 1. The resulting cage orbitals are ordered in shells in accordance with their spherical parentage as

$$a_{1g}(s) < t_{1u}(p) < h_g(d) \ll t_{2u}(f) \quad (1)$$

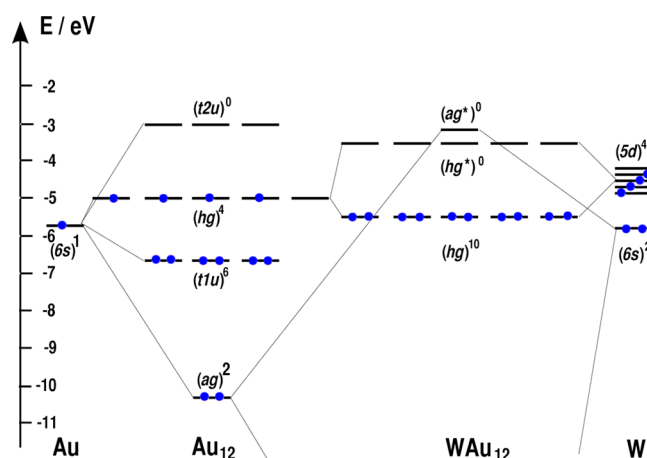


Figure 1. Orbital interactions in neutral W@Au_{12} within the relativistic zeroth-order approximation (ZORA).

A closed d -shell requires the magic number of 18 electrons. Since the $6s$ of gold is singly occupied, the gold clusters can only furnish 12 electrons for skeletal bonding. The role of the central tungsten atom, with valence shell $5d^6 6s^2$, is to furnish the remaining 6 electrons *via* hybridization between the $h_g(d)$ cluster MO on gold and the $5d$ orbitals on tungsten. The resulting h_g HOMO of the neutral species is fully occupied by 10 electrons and is of dominant Au $6s$ character. Its h_g^* LUMO counterpart is mainly of

Received: November 15, 2013

Published: December 23, 2013



W 5d character. The interaction also destabilizes the W 6s orbital, which becomes the next LUMO.

Li et al.⁵ produced the cluster by laser evaporation of a mixed Au/W target and recorded the photoelectron spectroscopy of $[W@Au_{12}]^-$. Comparison with relativistic DFT calculations corroborated the hypothesis of an icosahedral structure. So far attempts to produce the cluster in bulk have not been successful.⁶ In the monoanionic state the h_g^* LUMO is singly occupied, giving rise to a $5d^1$ configuration on tungsten. The resulting state is split by spin–orbit coupling into a Γ_8 quadruplet and a Γ_9 sextuplet, with parent j -values of 3/2 and 5/2, respectively. This cluster therefore constitutes a prime example of an icosahedral Jahn–Teller (JT) spin-problem in the presence of strong spin–orbit coupling.

2.2. $(\Gamma_8 + \Gamma_9) \times (g_g + 2h_g)$ Jahn–Teller Hamiltonian.

Previously we have constructed and solved the general JT Hamiltonian for the icosahedral d^9 configuration in the presence of spin–orbit coupling.¹ The JT part of the Hamiltonian was entirely attributed to the orbital instability: the fivefold degenerate d -orbitals transform as h_g and give rise to a $H_g \times (g_g + 2h_g)$ orbital JT problem. Addition of spin–orbit coupling transforms this into a $(\Gamma_8 + \Gamma_9) \times (g_g + 2h_g)$ problem. The spin–orbit ground state of a d^1 system is characterized by antiparallel coupling of orbital and spin moments and corresponds to the Γ_8 quadruplet. In d^9 the order is opposite with a Γ_9 ground state. The relevant distortion modes for h_g orbitals can lower the symmetry to D_{5d} and D_{3d} . These symmetries are intermediate symmetries or *epikernels* between the maximal I_h and minimal C_i symmetries of the Jahn–Teller energy surface.⁷ We will be concerned here with the first-order level splittings under small distortions of pentagonal and trigonal symmetry. The focus will be on the h_g part of the Hamiltonian which poses a challenging multiplicity problem.

The JT modes for an orbital quintuplet⁸ are obtained by taking the symmetrized part of the direct product $H_g \times H_g$, less the totally symmetric representation:

$$[H_g \times H_g] - a_g = g_g + 2h_g \quad (2)$$

The product multiplicity refers to the appearance of two h_g parts in the JT Hamiltonian. This means that there are two independent coupling channels between the orbital quintuplet and the h_g vibrations. The Clebsch–Gordan coupling coefficients on which the JT Hamiltonian is based thus separate into two linearly independent sets.⁹ Our resolution of this multiplicity problem is based on the embedding of the group of icosahedral rotations in the abstract S_6 permutation group containing all possible permutations of the six equivalent pentagonal directions in an icosahedron.^{2,10,11} In S_6 the set of pentagonal subgroups resolves into one totally symmetric and one fivefold degenerate irreducible representation, denoted as (6) and (5, 1) respectively. The (6) subduces the symmetric a_g representation, while the (5, 1) corresponds to the icosahedral h_g representation. Vice versa the five components of an orbital quintuplet can always be expressed as linear combinations of six pentagonal substates. The symmetrized part of the direct product $(5, 1) \times (5, 1)$ reads

$$[(5, 1) \times (5, 1)] - (6) = (5, 1) + (4, 2) \quad (3)$$

Comparison between the S_6 and I_h products yields the following branching scheme:

$$(4, 2) \rightarrow g_g + h_g(a)$$

$$(5, 1) \rightarrow h_g(b) \quad (4)$$

The two h_g coupling channels may thus be distinguished by their S_6 parentage. In the published coupling coefficients⁹ the multiplicity labels a and b have been chosen in accordance with this parentage.

The orbital JT Hamiltonian contains three force constants, denoted as F_{orb}^{Ha} , F_{orb}^{Hb} , and F_{orb}^G , corresponding to the three coupling schemes in Figure 2. In the standard D_2 basis of the h_g

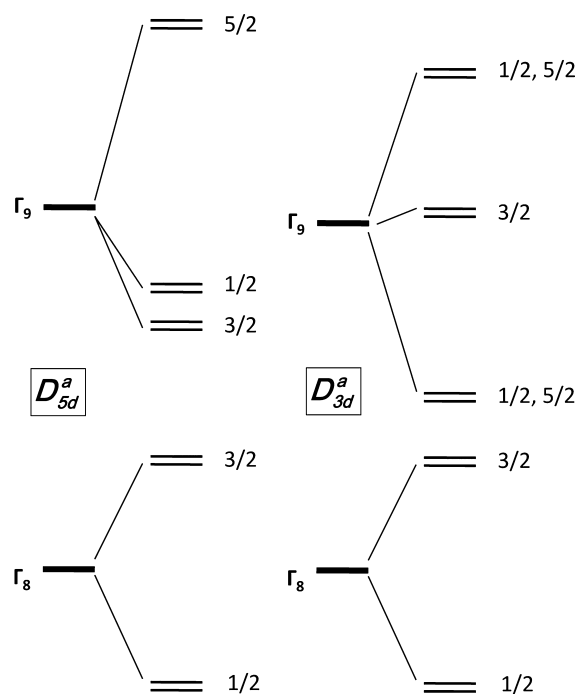


Figure 2. First-order JT splitting of the d^1 spin–orbit levels for pentagonal and trigonal distortions according to the $h_g(a)$ coupling channel.

representation, with components $\{h\theta, h\epsilon, h\xi, h\eta, h\zeta\}$, the pentagonal and trigonal distortion modes are expressed⁸ as

$$Q_{D_{5d}}^H = \frac{1}{\sqrt{10}}(\sqrt{3}Q_\theta - Q_\epsilon + \sqrt{6}Q_\eta)$$

$$Q_{D_{3d}}^H = \frac{1}{\sqrt{3}}(Q_\xi + Q_\eta + Q_\zeta) \quad (5)$$

The coordinate components must thus be inserted as

$$Q_\theta = \sqrt{3/10} Q_{D_{5d}}^H$$

$$Q_\epsilon = -\sqrt{1/10} Q_{D_{5d}}^H$$

$$Q_\eta = \sqrt{6/10} Q_{D_{5d}}^H \quad (6)$$

and

$$Q_\xi = \sqrt{1/3} Q_{D_{3d}}^H$$

$$Q_\eta = \sqrt{1/3} Q_{D_{3d}}^H$$

$$Q_\zeta = \sqrt{1/3} Q_{D_{3d}}^H \quad (7)$$

The tetrahedral distortion is defined along the Q_{Ga} mode. The tetrahedral distortions also belong to the epikernels of the distortion space but do not lead to a removal of the fourfold degeneracy of the ground state. As a result they are not JT active and will not be taken into consideration. To calculate the level splittings as a function of the F_{orb}^{Ha} and F_{orb}^{Hb} parameters we follow the procedure specified before.¹

2.3. Pentagonal and Trigonal $h_g(a)$ Coupling. In pentagonal symmetry the Γ_8 quadruplet is resolved into $E_{1/2g}$ and $E_{3/2g}$ sublevels, corresponding to pseudospin components 1/2 and 3/2 respectively. The Γ_9 sextuplet splits as $E_{1/2g} + E_{3/2g} + A_{5/2g} + A_{3/2g}^*$. From the general theory of the $(\Gamma_8 + \Gamma_9) \times (g_g + 2h_g)$ Jahn–Teller problem,¹ the first-order level splittings are written as

$$\begin{aligned}\Gamma_8: E(E_{1/2g}) &= -\frac{3}{10}F_{orb}^{Ha}Q_{D5d}^H \\ E(E_{3/2g}) &= \frac{3}{10}F_{orb}^{Ha}Q_{D5d}^H \\ \Gamma_9: E(E_{1/2g}) &= -\frac{1}{5}F_{orb}^{Ha}Q_{D5d}^H \\ E(E_{3/2g}) &= -\frac{3}{10}F_{orb}^{Ha}Q_{D5d}^H \\ E(A_{5/2g}) &= \frac{1}{2}F_{orb}^{Ha}Q_{D5d}^H\end{aligned}\quad (8)$$

For distortions along a trigonal mode the level splitting can be calculated with the Angular Overlap Matrix (AOM) technique, as explained before.¹ In this technique the H_g components are rotated to a trigonal frame, with the z' axis along the trigonal direction and the x' axis along a twofold direction. The JT energies of the complex d -orbitals in this frame are given by the following matrix in Table 1.

Table 1. Jahn–Teller Interaction Matrix for the Complex d -Orbitals in a Trigonal Frame

$F_{orb}^{Ha}Q_{D3d}^H$	$ H_g 0\rangle$	$ H_g \pm 1\rangle$	$ H_g \mp 2\rangle$
$\langle H_g 0 $	$-\frac{2}{3}$	0	0
$\langle H_g \pm 1 $	0	$-\frac{1}{18}$	$\mp \frac{5}{36\sqrt{2}} - i\frac{\sqrt{5}}{4\sqrt{6}}$
$\langle H_g \mp 2 $	0	$\mp \frac{5}{36\sqrt{2}} + i\frac{\sqrt{5}}{4\sqrt{6}}$	$\frac{7}{18}$

As can be seen here the $|\pm 1\rangle$ and $|\mp 2\rangle$ will be mixed as a result of the trigonal symmetry. The eigenvalues of this matrix are $(-2/3, +1/2, -1/6)$, in accordance with the results for the orbital treatment. At the spin–orbit level, this gives rise to an interaction element between the $|\pm 1/2\rangle$ and $|\mp 5/2\rangle$ components of the Γ_9 level, which in the D_{3d} double group both transform as $E_{1/2g}$. The spin–orbit components are defined as

$$\begin{aligned}|\Gamma_9 + 5/2\rangle &= |1/2\rangle|\alpha\rangle \\ |\Gamma_9 - 1/2\rangle &= \frac{\sqrt{2}}{\sqrt{5}}|-1\rangle|\alpha\rangle + \frac{\sqrt{3}}{\sqrt{5}}|0\rangle|\beta\rangle\end{aligned}\quad (9)$$

Both components will couple through the $\langle +2|\mathcal{H}_{JT}|-1\rangle$ orbital matrix element. Their interaction element reads

$$\langle \Gamma_9 + 5/2|\mathcal{H}_{JT}|\Gamma_9 - 1/2\rangle = \left(+\frac{\sqrt{5}}{36} + i\frac{1}{4\sqrt{3}} \right) F_{orb}^{Ha}Q_{D3d}^H \quad (10)$$

This off-diagonal element must be taken into account when calculating the energy splittings. The results are given by

$$\begin{aligned}\Gamma_8: E(E_{1/2g}) &= -\frac{3}{10}F_{orb}^{Ha}Q_{D3d}^H \\ E(A_{3/2g}) &= \frac{3}{10}F_{orb}^{Ha}Q_{D3d}^H \\ \Gamma_9: E(E_{1/2g}) &= \left(-\frac{1}{60} - \frac{\sqrt{3}\sqrt{227}}{60} \right) F_{orb}^{Ha}Q_{D3d}^H \\ E(A_{3/2g}) &= \frac{1}{30}F_{orb}^{Ha}Q_{D3d}^H \\ E(E_{1/2g}) &= \left(-\frac{1}{60} + \frac{\sqrt{3}\sqrt{227}}{60} \right) F_{orb}^{Ha}Q_{D3d}^H\end{aligned}\quad (11)$$

Comparison of the pentagonal and trigonal splitting patterns illustrates that the splitting of the Γ_8 level is isotropic. In contrast the Γ_9 level is anisotropic: it exhibits the largest slope, equal to $(1/2)F_{orb}^{Ha}$, for the $A_{5/2g}$ and $A_{3/2g}^*$ components along the pentagonal direction. The resulting model splittings are shown in Figure 2.

2.4. Pentagonal and Trigonal $h_g(b)$ Coupling. The b -type coupling channel is derived entirely in the same way, using the alternative set of coupling parameters. The results for the pentagonal splitting are

$$\begin{aligned}\Gamma_8: E(E_{1/2g}) &= -\frac{1}{2\sqrt{5}}F_{orb}^{Hb}Q_{D5d}^H \\ E(E_{3/2g}) &= \frac{1}{2\sqrt{5}}F_{orb}^{Hb}Q_{D5d}^H \\ \Gamma_9: E(E_{1/2g}) &= -\frac{1}{\sqrt{5}}F_{orb}^{Hb}Q_{D5d}^H \\ E(E_{3/2g}) &= \frac{1}{2\sqrt{5}}F_{orb}^{Hb}Q_{D5d}^H \\ E(A_{5/2g}) &= \frac{1}{2\sqrt{5}}F_{orb}^{Hb}Q_{D5d}^H\end{aligned}\quad (12)$$

For the trigonal distortion, the JT energies of the complex d -orbitals in the D_{3d} frame are given by the matrix in Table 2.

Table 2. Jahn–Teller Interaction Matrix for the Complex d -Orbitals in a Trigonal Frame

$F_{orb}^{Hb}Q_{D3d}^H$	$ H_g 0\rangle$	$ H_g \pm 1\rangle$	$ H_g \mp 2\rangle$
$\langle H_g 0 $	0	0	0
$\langle H_g \pm 1 $	0	$-\frac{\sqrt{5}}{6}$	$\pm \frac{\sqrt{5}}{12\sqrt{2}} + i\frac{\sqrt{3}}{4\sqrt{2}}$
$\langle H_g \mp 2 $	0	$\pm \frac{\sqrt{5}}{12\sqrt{2}} - i\frac{\sqrt{3}}{4\sqrt{2}}$	$\frac{\sqrt{5}}{6}$

The eigenvalues of this matrix are $(0, \pm 1/2)$, in accordance with the orbital quintuplet results. At the spin–orbit level, the trigonal field introduces an off-diagonal matrix element between the 1/2 and 5/2:

$$\langle \Gamma_9 + 5/2 | \mathcal{H}_{JT} | \Gamma_9 - 1/2 \rangle = \left(-\frac{1}{12} - i \frac{\sqrt{3}}{4\sqrt{5}} \right) F_{\text{orb}}^{Hb} Q_{D_{3d}} \quad (13)$$

The resulting first-order level splitting is given by

$$\begin{aligned} \Gamma_8: E(E_{1/2g}) &= -\frac{1}{2\sqrt{5}} F_{\text{orb}}^{Hb} Q_{D_{3d}} \\ E(A_{3/2g}) &= \frac{1}{2\sqrt{5}} F_{\text{orb}}^{Hb} Q_{D_{3d}} \\ \Gamma_9: E(E_{1/2g}) &= -\frac{1}{2\sqrt{5}} F_{\text{orb}}^{Hb} Q_{D_{3d}} \\ E(A_{3/2g}) &= -\frac{1}{2\sqrt{5}} F_{\text{orb}}^{Hb} Q_{D_{3d}} \\ E(E_{1/2g}) &= \frac{1}{\sqrt{5}} F_{\text{orb}}^{Hb} Q_{D_{3d}} \end{aligned} \quad (14)$$

As before the Γ_8 level is isotropic, while for the Γ_9 level the pentagonal and trigonal slopes are simply inverted. In the general diagram of the Γ_9 JT instability this corresponds to the mixing angle $\beta = \arccos(2/\sqrt{7})$.^{12,13} The resulting model splittings are shown in Figure 3.

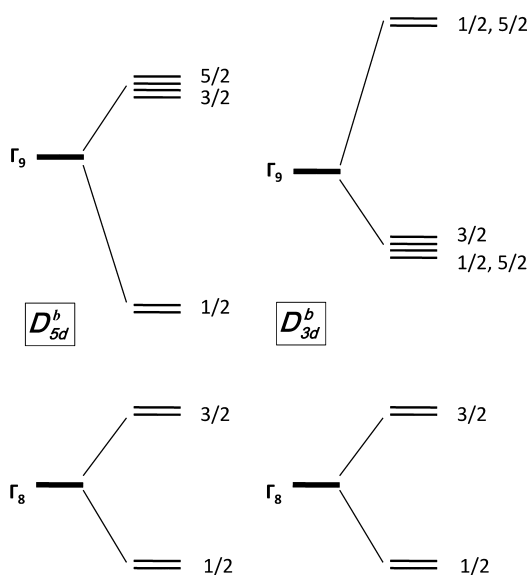


Figure 3. First-order JT splitting of the d^1 spin-orbit levels for pentagonal and trigonal distortions according to the $h_g(b)$ coupling channel.

2.5. Pentagonal and Trigonal h_g Distortions of the Au_{12} Cage. The icosahedral WAu_{12} cluster is positioned in a Cartesian frame with the z -axis along a pentagonal direction. Let R be the radius from the tungsten center to a gold atom. It is equal to 2.758154 au. The coordinates of the 12 gold atoms in units of R are given in Table 3. The z -axis is chosen along a pentagonal direction. The cluster is divided into three segments: the apical atoms (1,12) on the z -axis, a pentagonal upper ring (2–6), and pentagonal lower rings (7–11). The coordinates can conveniently be expressed by the following trigonometric functions:

$$\begin{aligned} \cos(2\pi/5) &= 1/(2\phi) \\ \sin(2\pi/5) &= (1/2)\sqrt{\sqrt{5}\phi} = (1/2)\alpha \end{aligned}$$

Table 3. Cartesian x, y, z Coordinates of the Icosahedral Vertices (units of $R\alpha^{-2}$) Expressed as a Function of ϕ and α

Apical Atoms (a)			
Au1	0	0	α^2
Au12	0	0	$-\alpha^2$
Upper Pentagon (u)			
Au2	$-\alpha\phi$	-1	ϕ
Au3	0	-2ϕ	ϕ
Au4	$\alpha\phi$	-1	ϕ
Au5	α	ϕ^2	ϕ
Au6	$-\alpha$	ϕ^2	ϕ
Lower Pentagon (l)			
Au7	$-\alpha$	$-\phi^2$	$-\phi$
Au8	α	$-\phi^2$	$-\phi$
Au9	$\alpha\phi$	1	$-\phi$
Au10	0	2ϕ	$-\phi$
Au11	$-\alpha\phi$	1	$-\phi$

where ϕ is the golden number.

In order to derive the orbital vibronic coupling constants by computational chemistry, one should perform small pentagonal and trigonal displacements from icosahedral symmetry and calculate the slopes. In principle a D_{5d} or D_{3d} distortion involves an arbitrary mixture of both a and b coupling channels, necessitating a numerical deconvolution of the energy profiles to obtain the separate F_{orb} -parameters. However, the case of the primitive icosahedral cage is special since it has only two vibrational modes of h_g symmetry that can easily be deconvoluted in the same S_6 parent group that also resolves the multiplicity problem. We call these the *canonical* symmetry modes and denote them as Q^{Ha} and Q^{Hb} . A distortion along one of these modes uniquely activates the corresponding coupling channel.

The derivation of the h_g -distortions of the Au_{12} cage and the corresponding S_6 -symmetry adaptation proceeds as follows. The icosahedron being a deltahedron, its vibrational modes span the symmetries of the 30 edges. In-phase combinations of antipodal edges gives rise to 15 *gerade* combinations, with symmetries $a_g + g_g + 2h_g$. These correspond to the set of JT-active modes. Now the icosahedron has six pentagonal directions, which are all adjacent. This set thus gives rise to 15 pairwise interactions between two pentagonal directions, and the scissoring mode between any pair will exactly match a *gerade* combination of antipodal edges. Permutations of pentagonal directions will thus induce permutations of the edges. As a consequence, the *gerade* vibrational modes can be assigned labels which express their permutational symmetry with respect to the S_6 group of all permutations of pentagonal directions. In this way the h_g distortion modes can directly be associated with the direct product of the pentagonal directions and thus can also be distinguished by the same a and b symmetry labels as were used for the product multiplicity separation. In Appendices A and B we derive the composition of these modes, both for pentagonal and for trigonal distortions. The coordinates are also expressed into Cartesian format, which can directly be introduced into the computational programs.

3. METHOD OF CALCULATION

We used the ADF2012 program package for the DFT calculations.¹⁴ We employed a generalized gradient approximation, Perdew–Wang exchange-correlation functional. The relativistic effect was taken into consideration within the scalar relativistic zero-order-regular approximation (ZORA).¹⁵ The

Slater-type-orbital (STO) basis sets were employed including triple- ζ plus polarization functions (TZP) for the valence orbitals of all the atoms. The optimizations were performed under the criterion of energy gradient converging to 10^{-4} Hartree Å. The frozen core approximation to the $[1s^2-4f^4]$ core of W and the $[1s^2-4d^{10}]$ core of Au was employed.

Since I_h symmetry is not implemented in ADF 2012, the neutral molecule was treated with the D_{5d} subgroup symmetry. As mentioned before, under the D_{5d}^* double group, the quadruplet and sextuplet representations are

$$\Gamma_8 \downarrow D_{5d}^* = E_{3/2g} \oplus E_{1/2g} \quad (15)$$

$$\Gamma_9 \downarrow D_{5d}^* = A_{5/2g} \oplus A_{5/2g}^* \oplus E_{3/2g} \oplus E_{1/2g} \quad (16)$$

The optimization of the neutral state with D_{5d} symmetry is performed within the scalar relativistic ZORA. Since an analytical frequency calculation is not implemented for the PW91 exchange-correlation functional, the vibrational analysis of the neutral state was performed numerically. In the calculations for the anion, spin-orbit couplings were included. For the calculation of the anionic state, we treated the degenerate HOMO levels with fractional occupation as tabulated in Table 4.

Table 4. Occupation Numbers of the Frontier Γ_8 and Γ_9 Levels

	I_h^*		D_{5d}^*		D_{3d}^*
Γ_8	1.00	$E_{3/2g}(24)$	0.50	$A_{3/2g}(21)$	0.25
		$E_{1/2g}(28)$	0.50	$A_{3/2g}^*(21)$	0.25
				$E_{1/2g}(42)$	0.50
Γ_9	0.00	$A_{5/2g}(12)$	0.00	$E_{1/2g}(44)$	0.00
		$A_{5/2g}^*(12)$	0.00	$A_{3/2g}(22)$	0.00
		$E_{3/2g}(25)$	0.00	$A_{3/2g}^*(22)$	0.00
		$E_{1/2g}(30)$	0.00	$E_{1/2g}(45)$	0.00

Single-point calculations including the spin-orbit couplings were performed along the h_g canonical modes, Q^{Ha} and Q^{Hb} . The two separate coupling channels can be explored by following the canonical modes. The orbital vibronic coupling constants were calculated from the energy gradients of the orbital levels as a function of the canonical mode. The spin-orbit coupling constant ζ is estimated from the level splitting at the Jahn–Teller crossing point.

4. RESULTS AND DISCUSSION

The optimized geometry and the vibrational modes are shown in Tables S1 and S2 of the Supporting Information. The molecular orbitals within the ZORA and with the spin-orbit coupling are shown in Figures 4 and 5, respectively.

4.1. Spin–Orbit Coupling. Orbital levels without the spin-orbit coupling are tabulated in Table 5. The orbital levels of the anionic state at the Jahn–Teller crossing point with the I_h symmetry, the optimized structure of the neutral state, is tabulated in Table 6. The representations of the orbital levels shown in Table 6 are those of D_{5d}^* because of the program limitation. $E_{1/2g}(29)$ level in between the Γ_8 and Γ_9 levels is an antibonding orbital between the Au_{12} cage orbital and W 6s orbital which is not Jahn–Teller active. Since the spin-orbit coupling constant ζ satisfies the equation

$$\Delta E = E_{\Gamma_9} - E_{\Gamma_8} = \frac{5}{2}\zeta \quad (17)$$

the spin-orbit coupling constant is obtained as

$$\zeta = 125.1 \text{ meV} \quad (18)$$

Table 5. Orbital Levels of the Anion at the Jahn–Teller Crossing Point without the Spin-Orbit Coupling

orbital		occupation	orbital energy in eV
I_h	$\downarrow D_{5d}$		
h_g	$e_{2g}(11)$	4.00	−1.9725
	$e_{1g}(12)$	4.00	−1.9725
	$a_{1g}(12)$	2.00	−1.9725
a_g	$a_{1g}(13)$	0.00	−0.2418
h_g^*	$e_{2g}(12)$	0.40	−0.1765
	$e_{1g}(13)$	0.40	−0.1765
	$a_{1g}(14)$	0.20	−0.1765
t_{2u}	$e_{2u}(11)$	0.00	0.3223
	$a_{2u}(12)$	0.00	0.3223

Table 6. Orbital Energy Levels at the Jahn–Teller Crossing Point $Q^{Ha} = 0.0$, $Q^{Hb} = 0.0$

	level	occupation	orbital energy in eV
Γ_8	$E_{3/2g}(24)$	0.50	−0.3549
	$E_{1/2g}(28)$	0.50	−0.3549
	$E_{1/2g}(29)$	0.00	−0.2345
Γ_9	$A_{5/2g}(12)$	0.00	−0.0422
	$A_{5/2g}^*(12)$	0.00	−0.0422
	$E_{3/2g}(25)$	0.00	−0.0422
	$E_{1/2g}(30)$	0.00	−0.0421

The spin-orbit coupling parameter ζ_{5d} for atomic tungsten amounts to 260 meV. The calculated value is only about half of this value. This quenching is attributed to hybridization between the central transition-metal and the gold cage (Figures 4 and 5).

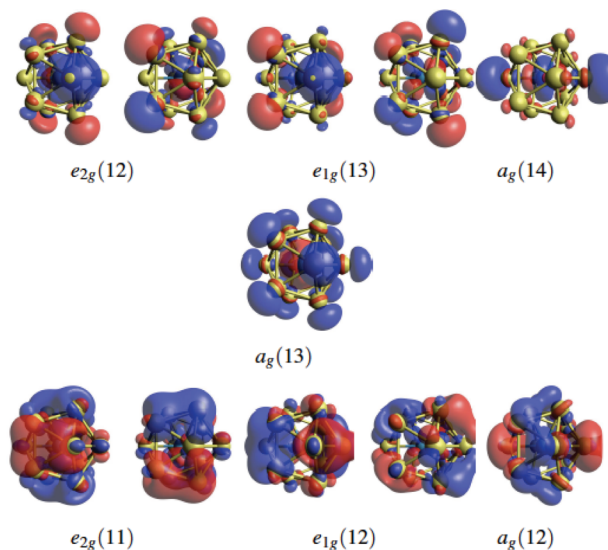


Figure 4. Molecular orbitals of $[WAu_{12}]^-$ within the ZORA.

4.2. JT Splittings. **4.2.1. $h_g(a)$ Coupling.** As explained before, we calculated the JT splittings of the anionic ground and excited states under pentagonal and trigonal distortions. The two coupling channels are evaluated separately by applying the appropriate canonical distortion modes. In Table 7, the orbital energy gradients for the pentagonal $H_g a$ canonical mode are compared to the slopes predicted by the orbital model (see eq 8 and eq 11). The corresponding orbital vibronic coupling constants (OVCC) are extracted by dividing the energy gradient by the slope.

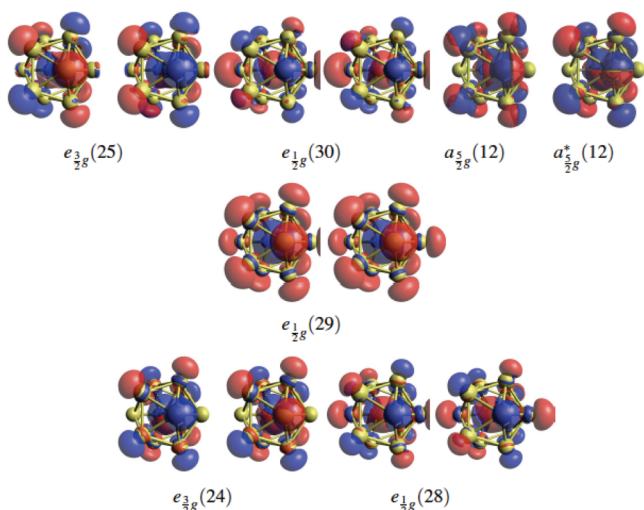


Figure 5. Molecular orbitals of $[\text{WAu}_{12}]^-$ considering spin–orbit coupling.

The orbital vibronic coupling constants were estimated from the orbital energy gradients. In the simple orbital approximation a single coupling constant should describe all gradients. For the occupied levels, $E_{3/2g}(24)$ and $E_{1/2g}(28)$, the calculated values almost coincide with an average of 0.223 eV/\AA . On the other hand, for the virtual Γ_9 levels the fit is less satisfying. The largest deviation is found for the $A_{3/2g}(22)$ level. This level is characterized by the smallest slope and thus most susceptible to numerical uncertainties and second-order effects.

In any case the JT splitting of all spin–orbit levels shows a satisfying semiquantitative agreement with the simple orbital model. The predicted equality of the OVCC for the trigonal and pentagonal distortions is also remarkably well reproduced. Figures 6 and 7 show the orbital level splittings for the pentagonal and trigonal distortions along the canonical Q^{Ha} mode. The calculated splitting schemes reflect very well the model schemes of Figure 2.

4.3. $h_g(b)$ Coupling. In Table 8 we present the results for the $h_g(b)$ coupling scheme. The corresponding slopes are provided in eq 12. The agreement with the predictions based on the orbital model is very good, except for the Γ_9 components $E_{3/2g}(25)$ and $A_{5/2g}(12)$. According to the model both should remain quasi-degenerate and rise with a slope of 0.223. In fact the 3/2 component rises twice as fast, while the 5/2 component has a small negative slope. This gives the impression that the quasi-degeneracy has introduced a numerical instability in the calculation. All other values are in line with the predictions.

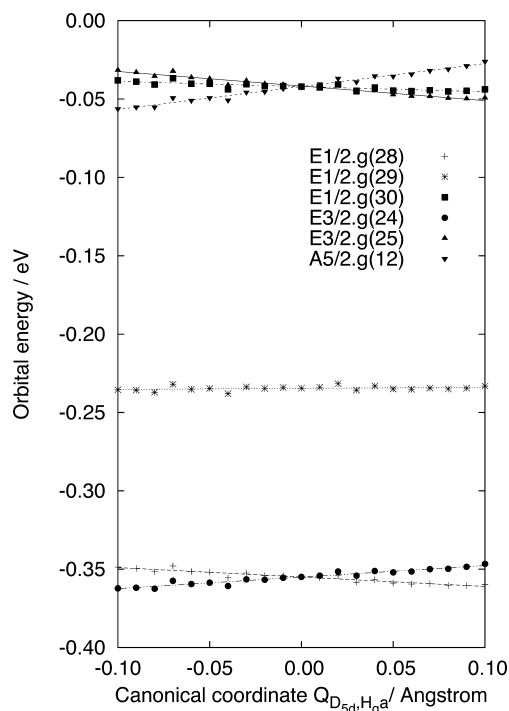


Figure 6. Orbital level splitting for the pentagonal distortion of the canonical Q_{D5d}^{Ha} mode. The lines are results of the least-squares fittings.

From the occupied states the average OVCC for the b -channel is 0.272 eV/\AA , which is slightly higher than the value for the a -channel, and points to a preference for a pentagonal distortion. In Figures 8 and 9 the calculated splitting schemes are shown. These can directly be compared to the model schemes in Figure 3. In all diagrams the $6s$ intruder level is almost not affected by the JT distortions, which is as expected for the first-order response of orbitally nondegenerate levels.

5. JT MINIMUM

The foregoing treatment was concerned with the first-order JT splittings in the immediate vicinity of the icosahedral degeneracy point. We did also examine the energy minimum of the JT hypersurface along the pentagonal directions. At larger distortions the orbital energy effects become dominant over the spin–orbit energy. From the structure of the minimum one can often infer what are the important bonding contributions that are at the origin of the JT effect.

The minimal pentagonal structure is found along the positive Q_{D5d}^{Ha} distortion and is shown in Figure 10. This structure is quite different from the icosahedral starting geometry and has a special

Table 7. Orbital Energy Gradient for the Pentagonal and Trigonal Q^{Ha} Canonical Modes and Corresponding OVCC

		orbital energy gradient ($\text{meV}\cdot\text{\AA}^{-1}$)	slope	OVCC ($\text{meV}\cdot\text{\AA}^{-1}$)
Q_{D5d}^{Ha}	$E_{3/2g}(24)$	74(4)	0.3	245
	$E_{1/2g}(28)$	−60(5)	−0.3	201
	$A_{5/2g}(12)$	146(5)	0.5	293
	$E_{3/2g}(25)$	−93(5)	−0.3	310
	$E_{1/2g}(30)$	−33(5)	−0.2	166
	$E_{1/2g}(42)$	−70(4)	−0.300	234
Q_{D3d}^{Ha}	$A_{3/2g}(21)$	64(4)	0.300	214
	$E_{1/2g}(44)$	111(5)	0.418	265
	$A_{3/2g}(22)$	18(5)	0.033	528
	$E_{1/2g}(45)$	−136(5)	−0.452	300

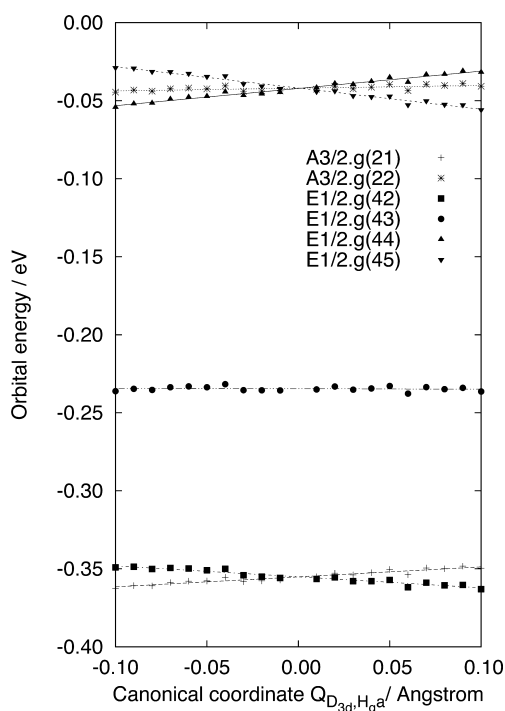


Figure 7. Orbital level splitting for the trigonal distortion of the canonical Q_{D3d}^{Ha} mode. The lines are results of the least-squares fittings.

interest in its own right. It indeed resembles a sandwich compound. In the ferrocene standard model, the cyclopentadienyl ligand caps are counted as anionic ligand caps, each containing a 6π aromatic sextet, leaving a Fe^{2+} central metal with six d -electrons. The structure in Figure 10 contains two pentagonal pyramidal Au_6 caps. They contain six valence electrons occupying three bonding orbitals, yielding a $\sigma^2\pi^4$ configuration which is isolobal to an aromatic sextet. Moreover the zerovalent W -center provides six more electrons, exactly as Fe^{2+} . From this point of view one could postulate the existence of a closed shell $W(\eta^5Au_6)_2$ alternative to the endohedral compound. The latter apparently is more stable though, in view of the magic number rule for spherical clusters. However the anionic $[WAu_{12}]^-$ cluster has one extra antibonding electron which tears the cage apart. If this electron would enter the $d\pi$ -antibonding level, like in the ferrocene anion, a further JT distortion would be expected, leading probably to a bent structure. In the present case, a way out to accommodate the extra electron is the intermediate $6s$ level which is totally symmetric and will not disrupt the sandwich structure.

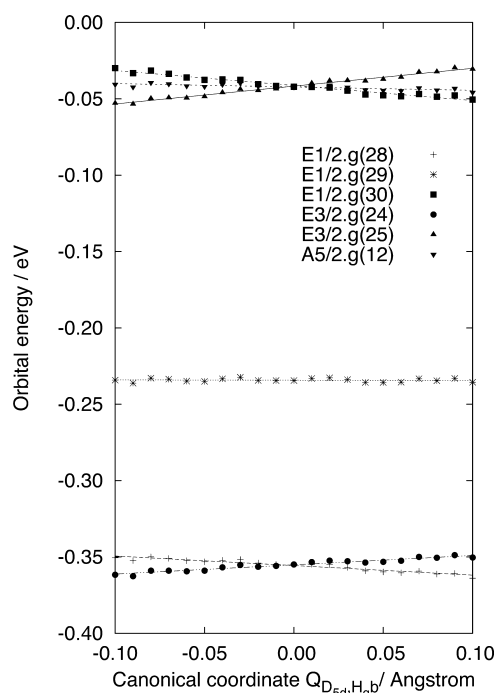


Figure 8. Orbital level splitting for the pentagonal distortion of the canonical Q_{D5d}^{Hb} mode. The lines are results of the least-squares fittings.

6. CONCLUSION

Our study of the JT instability in the anionic gold–tungsten cluster has served a double purpose. For one, it has provided the opportunity for a detailed computational analysis of the Jahn–Teller instability in fourfold and sixfold degenerate icosahedral spinors. The results provide a very good agreement with a model treatment based on orbital vibronic coupling. This is the first time that the group-theoretical results for this intricate JT problem could be checked by direct calculation. An evident extension of this work would be to investigate the cationic cluster as well, since this is predicted to have a h_g^9 configuration, which would be characterized by a Γ_9 ground state.

Following the JT distortions further to a regime where the orbital characteristics become more pronounced, the study also yielded another interesting conclusion. It generated an alternative bonding situation, resembling a sandwich complex. In the pentagonal JT minimum a six-atom gold cluster is seen to form a flattened pentagonal pyramid, with an aromatic sextet count, which is stabilized by its interaction with a transition-metal center. Further explorations of such coordinative structures will certainly be interesting. Since the Jahn–Teller couplings would

Table 8. Orbital Energy Gradients and F_{orb}^{Hb} for the Pentagonal and Trigonal Q^{Hb} Canonical Mode

		orbital energy gradient (meV·Å ⁻¹)	slope	OVCC F_{orb}^{Hb} (meV·Å ⁻¹)
Q_{D5d}^{Ha}	$E_{3/2g}(24)$	61(4)	0.223	272
	$E_{1/2g}(28)$	−63(4)	−0.223	281
	$E_{3/2g}(25)$	117(4)	0.223	521
	$A_{5/2g}(12)$	−22(4)	0.223	−98
	$E_{1/2g}(30)$	−98(4)	−0.447	220
	$E_{1/2g}(42)$	−61(6)	−0.223	274
Q_{D3d}^{Ha}	$A_{3/2g}(21)$	58(5)	0.223	260
	$E_{1/2g}(44)$	123(5)	0.447	275
	$A_{3/2g}(22)$	−72(5)	−0.223	323
	$E_{1/2g}(45)$	−55(5)	−0.223	246

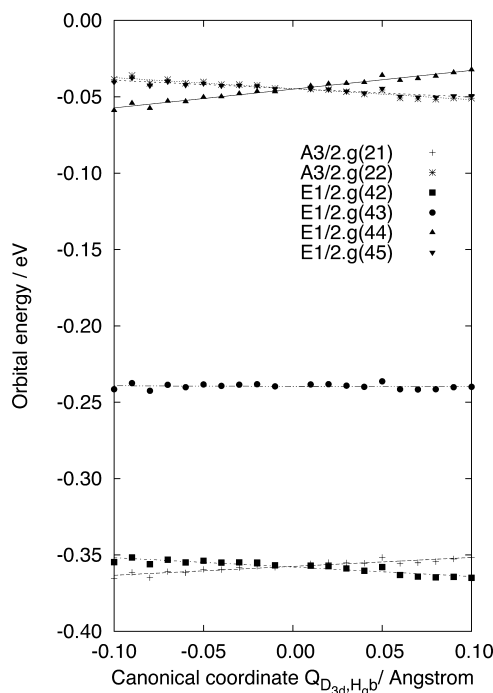


Figure 9. Orbital level splitting for the trigonal distortion of the canonical $Q_{D_{3d}}^{Hb}$ mode. The lines are results of the least-squares fittings.

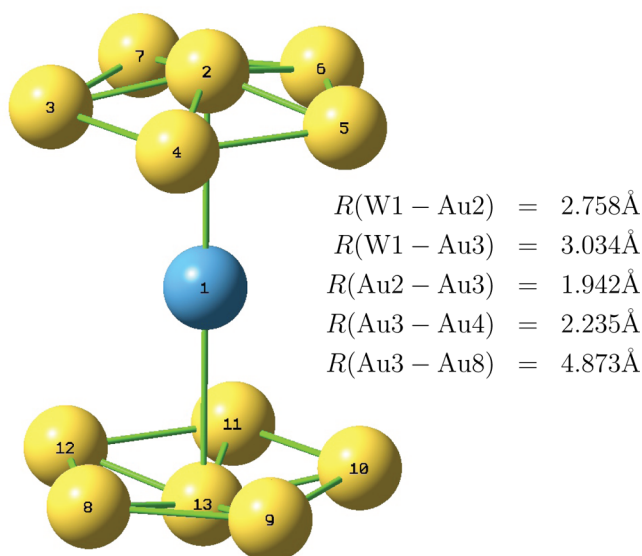


Figure 10. Minimal pentagonal JT structure.

quench the orbital contribution to the magnetic moment, we could expect the observable effect on the g-factors in electron paramagnetic resonance (EPR) spectroscopy.

■ APPENDIX A: CANONICAL PENTAGONAL MODES

In pentagonal D_{5d} symmetry the 30 edges form three separate orbits: edges which connect the apex atoms to the pentagonal rings, edges along the pentagonal rings, and edges which connect the upper and lower ring across the equator. We will label these orbits as (a,u) , (u,u) , and (u,l) , respectively. Each orbit contains 10 edges. From these orbits three modes may be constructed which are totally symmetric in D_{5d} .

$$\Delta_{a,u} = \Delta r_{1,2} + \Delta r_{1,3} + \Delta r_{1,4} + \Delta r_{1,5} + \Delta r_{1,6} + \Delta r_{12,7} + \Delta r_{12,8} + \Delta r_{12,9} + \Delta r_{12,10} + \Delta r_{12,11}$$

$$\Delta_{u,u} = \Delta r_{2,3} + \Delta r_{3,4} + \Delta r_{4,5} + \Delta r_{5,6} + \Delta r_{6,2} + \Delta r_{7,8} + \Delta r_{8,9} + \Delta r_{9,10} + \Delta r_{10,11} + \Delta r_{11,7}$$

$$\Delta_{u,l} = \Delta r_{2,7} + \Delta r_{7,3} + \Delta r_{3,8} + \Delta r_{8,4} + \Delta r_{4,9} + \Delta r_{9,5} + \Delta r_{5,10} + \Delta r_{10,6} + \Delta r_{6,11} + \Delta r_{11,2}$$

These three edge sets give rise to three symmetrized coordinates, with icosahedral parentages $a_g + 2h_g$. The totally symmetric coordinate is of course the breathing mode, which is simply the total summation over all edges:

$$Q_{Ih}^{A_g} = \frac{1}{\sqrt{30}}(\Delta_{a,u} + \Delta_{u,u} + \Delta_{u,l}) \quad (19)$$

where normalization runs over the 30 edges. The h_g symmetrized coordinates are denoted by multiplicity labels a and b , which refer to the S_6 parentage of the interactions between the six pentagonal directions. Using the Clebsch–Gordan coupling coefficients for $h_g \times h_g = 2h_g$ these can be obtained as follows:

$$Q_{D5d}^{Ha} = \frac{1}{\sqrt{20}}(\Delta_{u,u} - \Delta_{u,l})$$

$$Q_{D5d}^{Hb} = \frac{1}{\sqrt{60}}(2\Delta_{a,u} - \Delta_{u,u} - \Delta_{u,l})$$

We will refer to these basis vectors as the canonical coordinates of the pentagonal distortion space. In the a -mode the Au_{12} cage is deformed into two flattened Au_6 caps at opposite poles of the pentagonal axis (see Figure 10). In the b -mode the bonds to apical atoms are elongated, leaving a compressed Au_{10} pentagonal antiprism in the middle. In reference to the earlier work of Boyle and Parker¹⁶ and of Vos et al.,¹⁷ we can also compare the results with the totally symmetric pentagonal components of the ν_6 and ν_7 modes of H_g symmetry. The projection of the a_{1g} pentagonal component in the H_g quintuplet manifold is given in eq 5. Applying this projection to the ν_6 mode given in the work of Vos yields:

$$Q_{D5d}^{\nu_6} = \frac{1}{\sqrt{60}}(-\Delta_{a,u} - \Delta_{u,u} + 2\Delta_{u,l}) \quad (20)$$

Clearly this component corresponds to an element of the pentagonal distortion space. It can easily be expressed in the canonical components as

$$Q_{D5d}^{\nu_6} = -\frac{\sqrt{3}}{2}Q_{D5d}^{Ha} - \frac{1}{2}Q_{D5d}^{Hb} \quad (21)$$

For the ν_7 coordinate the results are as follows:

$$\begin{aligned} Q_{D5d}^{\nu_7} &= \frac{1}{\sqrt{20}}(\Delta_{a,u} - \Delta_{u,u}) \\ &= -\frac{1}{2}Q_{D5d}^{Ha} + \frac{\sqrt{3}}{2}Q_{D5d}^{Hb} \end{aligned}$$

To prepare the input for the ADF calculations we must convert the changes of the bond lengths Δr_{ij} between atoms i and j into Cartesian displacements of these atoms, denoted as x_i, y_i, z_i etc., and the equilibrium positions, given in Table 3, and denoted as X_i^0, Y_i^0, Z_i^0 .

$$\Delta r_{ij} = (X_j^0 - X_i^0)(x_j - x_i) + (Y_j^0 - Y_i^0)(y_j - y_i) + (Z_j^0 - Z_i^0)(z_j - z_i) \quad (22)$$

It is convenient to divide these expressions by R to obtain dimensionless quantities. We now combine the Cartesian starting positions with the expressions for the canonical pentagonal distortions of h_g symmetry to obtain Cartesian displacement vectors for all atoms. The results are given in Tables 9 and 10 for respectively the Q_{D3d}^{Ha} and Q_{D3d}^{Hb} modes. Due to

Table 9. Normalized Cartesian Displacement Vectors for the Q^{Ha} Pentagonal Distortion (units of $(\sqrt{40}\alpha^2)^{-1}$)

Apical Atoms (a)			
Au1	0	0	0
Au12	0	0	0
Upper Pentagon (u)			
Au2	$-\alpha\phi$	-1	-4ϕ
Au3	0	-2ϕ	-4ϕ
Au4	$\alpha\phi$	-1	-4ϕ
Au5	α	ϕ^2	-4ϕ
Au6	$-\alpha$	ϕ^2	-4ϕ
Lower Pentagon (l)			
Au7	$-\alpha$	$-\phi^2$	4ϕ
Au8	α	$-\phi^2$	4ϕ
Au9	$\alpha\phi$	1	4ϕ
Au10	0	2ϕ	4ϕ
Au11	$-\alpha\phi$	1	4ϕ

Table 10. Normalized Cartesian Displacement Vectors for the Q^{Hb} Pentagonal Distortion (units of $(2\sqrt{90} - 24\sqrt{5}\alpha^2)^{-1}$)

Apical Atoms (a)			
Au1	0	0	20
Au12	0	0	-20
Upper Pentagon (u)			
Au2	$-\alpha\phi^{-2}$	$-\phi^{-3}$	$-4\phi^2$
Au3	0	$-2\phi^{-2}$	$-4\phi^2$
Au4	$\alpha\phi^{-2}$	$-\phi^{-3}$	$-4\phi^2$
Au5	$\alpha\phi^{-3}$	ϕ^{-1}	$-4\phi^2$
Au6	$-\alpha\phi^{-3}$	ϕ^{-1}	$-4\phi^2$
Lower Pentagon (l)			
Au7	$-\alpha\phi^{-3}$	$-\phi^{-1}$	$4\phi^2$
Au8	$\alpha\phi^{-3}$	$-\phi^{-1}$	$4\phi^2$
Au9	$\alpha\phi^{-2}$	ϕ^{-3}	$4\phi^2$
Au10	0	$2\phi^{-2}$	$4\phi^2$
Au11	$-\alpha\phi^{-2}$	ϕ^{-3}	$4\phi^2$

the nonunitary transformation from internal to Cartesian coordinates, the transformed canonical modes are no longer orthogonal in Cartesian space. Their exact directions in the orthogonal framework of Q_1^H and Q_2^H modes from the ADF calculations are shown in Figure 11.

■ APPENDIX B: CANONICAL TRIGONAL MODES

The h_g distortion modes also give rise to a trigonal epikernel group of D_{3d} symmetry. In this symmetry the 12 vertices are resolved into two orbits: an upper and a lower triangle, and a puckered hexagonal ring around the equator. If we take the three vertices 1, 2, 3 as the upper triangle, the equator ring consists of the vertices 4, 5, 6, 11, 7, 8 and the remaining three 9, 10, 12 form the lower triangle. The set of 30 vertices separates into four

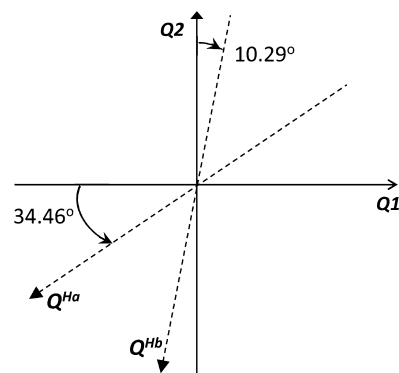


Figure 11. Relationship between the canonical modes Q^{Ha} , Q^{Hb} and the orthonormal H_g -type symmetry coordinates Q_1^H , Q_2^H provided by ADF.

Table 11. Normalized Cartesian Displacement Vectors for the Q^{Ha} Trigonal Distortion (units of $(\sqrt{72}\alpha^2)^{-1}$)

Upper Triangle			
Au1	$-\alpha(\phi + 2)$	$-(4\phi + 3)$	0
Au2	$2\alpha\phi$	$-2(\phi + 1)$	$\alpha^2 + 3\phi$
Au3	$-\alpha(\phi + 2)$	$2\phi + 1$	$\alpha^2 + 3\phi$
Equator			
Au4	$-2\alpha(\phi - 1)$	-2	2ϕ
Au5	$\alpha(\phi - 1)$	ϕ	$-2(\alpha^2 - \phi)$
Au6	$-\alpha(\phi - 1)$	$-(3\phi - 2)$	2ϕ
Au7	$-\alpha(\phi - 1)$	$-\phi$	$2(\alpha^2 - \phi)$
Au8	$\alpha(\phi - 1)$	$3\phi - 2$	-2ϕ
Au11	$2\alpha(\phi - 1)$	2	-2ϕ
Lower Triangle			
Au9	$-2\alpha\phi$	$2(\phi + 1)$	$-(\alpha^2 + 3\phi)$
Au10	$\alpha(\phi + 2)$	$-(2\phi + 1)$	$-(\alpha^2 + 3\phi)$
Au12	$\alpha(\phi + 2)$	$4\phi + 3$	0

orbits, which we will designate as $\Delta_{t,t}$, $\Delta_{e,e}$, $\Delta_{t,e}$, $\Delta'_{t,e}$. They are defined as follows:

$$\Delta_{t,t} = \Delta r_{1,2} + \Delta r_{2,3} + \Delta r_{3,1} + \Delta r_{9,10} + \Delta r_{10,12} + \Delta r_{12,9}$$

$$\Delta_{e,e} = \Delta r_{4,5} + \Delta r_{5,6} + \Delta r_{6,11} + \Delta r_{11,7} + \Delta r_{7,8} + \Delta r_{8,4}$$

$$\Delta_{t,e} = \Delta r_{1,5} + \Delta r_{2,11} + \Delta r_{3,8} + \Delta r_{4,9} + \Delta r_{6,10} + \Delta r_{7,12}$$

$$\Delta'_{t,e} = \Delta r_{1,4} + \Delta r_{1,6} + \Delta r_{2,6} + \Delta r_{2,7} + \Delta r_{3,7} + \Delta r_{3,4} + \Delta r_{5,9} + \Delta r_{9,8} + \Delta r_{5,10} + \Delta r_{10,11} + \Delta r_{11,12} + \Delta r_{8,12}$$

As before canonical modes will be distinguished by their permutational symmetry in the group S_6 . The multiplicity labels a and b will again designate components which belong to the irreducible representations $[4,2]$ and $[5,1]$, respectively. One has

$$Q_{D3d}^{Ha} = \frac{1}{6}(2\Delta_{t,e} - \Delta_{t,t} - \Delta_{e,e})$$

$$Q_{D3d}^{Hb} = \frac{1}{2\sqrt{3}}(\Delta_{t,t} - \Delta_{e,e})$$

We can again compare these results with the totally symmetric trigonal components of the ν_6 and ν_7 modes of H_g symmetry in the Boyle and Parker coordinates. One obtains

Table 12. Normalized Cartesian displacement vectors for the Q^{Hb} trigonal distortion (units of $1/(\sqrt{72} - (96/\sqrt{5})\alpha^2)$)

Upper Triangle			
Au1	$\alpha\phi$	$2\phi + 1$	$2(\alpha^2 - \phi)$
Au2	$-2\alpha\phi$	$2(\phi - 1)$	$-(\alpha^2 - \phi)$
Au3	$\alpha\phi$	$-(4\phi - 1)$	$-(\alpha^2 - \phi)$
Equator			
Au4	$-2\alpha(\phi - 1)$	2	-2ϕ
Au5	$\alpha(\phi - 3)$	$-(\phi + 2)$	0
Au6	$-\alpha(\phi - 3)$	$-\phi$	-2ϕ
Au7	$-\alpha(\phi - 3)$	$\phi + 2$	0
Au8	$\alpha(\phi - 3)$	ϕ	2ϕ
Au11	$2\alpha(\phi - 1)$	-2	2ϕ
Lower Triangle			
Au9	$2\alpha\phi$	$-2(\phi - 1)$	$\alpha^2 - \phi$
Au10	$-\alpha\phi$	$4\phi - 1$	$\alpha^2 - \phi$
Au12	$-\alpha\phi$	$-(2\phi + 1)$	$-2(\alpha^2 - \phi)$

$$Q_{D3d}^{v_6} = \frac{1}{2\sqrt{3}}(-\Delta_{t,t} + \Delta_{t,e})$$

$$Q_{D3d}^{v_7} = \frac{1}{6}(\Delta_{t,t} + \Delta_{t,e} - 2\Delta_{e,e})$$

Again these can be redistributed over the canonical components yielding exactly the same relationships as in eq 22. Further proceeding in the same way as before, we can convert the canonical trigonal h_g modes into Cartesian coordinates. The results are given in Tables 11 and 12 for respectively the Q^{Ha} and Q^{Hb} modes.

■ ASSOCIATED CONTENT

● Supporting Information

(1) Optimized geometry; (2) vibrational mode. This material is available free of charge via the Internet at <http://pubs.acs.org>.

■ AUTHOR INFORMATION

Corresponding Author

*E-mail: tsato@moleng.kyoto-u.ac.jp.

Notes

The authors declare no competing financial interest.

■ ACKNOWLEDGMENTS

Theoretical calculations were partly performed using Research Center for Computational Science, Okazaki, Japan, and the Supercomputer Laboratory of Institute for Chemical Research, Kyoto University. Financial support from the JSPS (the Japan Society for the Promotion of Science)-FWO (Fonds voor Wetenschappelijk Onderzoek-Vlaanderen) bilateral program is gratefully acknowledged. The present work was partially supported by MEXT program "Elements Strategy Initiative to Form Core Research Center" (since 2012), MEXT; Ministry of Education Culture, Sports, Science and Technology, Japan.

■ REFERENCES

- (1) Sato, T.; Ceulemans, A. *J. Chem. Phys.* **2007**, *126*, 184501-1-9.
- (2) Lijnen, E.; Ceulemans, A. *EPL* **2007**, *80*, 67006-1-4.
- (3) Pyykkö, P.; Runeberg, N. *Angew. Chem., Int. Ed.* **2002**, *41*, 2174-2176.
- (4) Autschback, J.; Hess, B. A.; Johansson, M. P.; Neugebauer, J.; Patzschke, M.; Pyykkö, P.; Sundholm, D. *Phys. Chem. Chem. Phys.* **2004**, *11*, 11-22.

- (5) Li, X.; Kiran, B.; Li, J.; Zhai, H.-J.; Wang, L.-S. *Angew. Chem., Int. Ed.* **2002**, *41*, 4786-4789.
- (6) Johansson, M. P.; Pyykkö, P. *Chem. Commun.* **2010**, *46*, 3762-3764.
- (7) Ceulemans, A.; Vanquickenborne, L. G. *Struct. Bonding (Berlin)* **1989**, *71*, 125-159.
- (8) Ceulemans, A.; Fowler, P. W. *J. Chem. Phys.* **1990**, *93*, 1221-1234.
- (9) Fowler, P. W.; Ceulemans, A. *Mol. Phys.* **1985**, *54*, 767-785.
- (10) Ceulemans, A.; Lijnen, E. *Bull. Chem. Soc. Jpn.* **2007**, *80*, 1229-1240.
- (11) Ceulemans, A.; Lijnen, E. In *Electronic Degeneracy and Vibrational Degrees of Freedom: The Permutational Proof of the Jahn-Teller Theorem*; Koppel, H., Yarkony, D. R., Barentzen, H., Eds.; Springer Series in Chemical Physics; Springer-Verlag: Heidelberg, 2009; Vol. 97, pp 25-50.
- (12) Ceulemans, A.; Lijnen, E.; Qiu, Q.-C. *ChemPhysChem* **2007**, *8*, 64-67.
- (13) Qiu, Q.-C.; Lijnen, E.; Ceulemans, A. *Mol. Phys.* **2006**, *104*, 3171-3185.
- (14) ADF2012.01. SCM, *Theoretical Chemistry*, Vrije Universiteit: Amsterdam, The Netherlands, 2012.
- (15) van Lenthe, E.; Baerends, E. J.; Snijders, J. G. *J. Chem. Phys.* **1993**, *99*, 4597-4610.
- (16) Boyle, L. L.; Parker, Y. M. *Mol. Phys.* **1980**, *39*, 95-109.
- (17) Ceulemans, A.; Titeca, B. C.; Chibotaru, L. F.; Vos, I.; Fowler, P. W. *J. Phys. Chem. A* **2001**, *36*, 8284-8295.